Rapid Communications

Emergence of topologically protected states in the $MoTe_2$ Weyl semimetal with layer-stacking order

John A. Schneeloch,[1] Chunruo Duan,[1] Junjie Yang,[1,*] Jun Liu,[2] Xiaoping Wang,[3] and Despina Louca[1,†]

[1]*Department of Physics, University of Virginia, Charlottesville, Virginia 22904, USA*

[2]*Division of Materials Science and Engineering, Ames Laboratory, Ames, Iowa 50011, USA*

[3]*Chemical and Engineering Materials Division, Oak Ridge National Laboratory, Oak Ridge, Tennessee 37831, USA*

(Received 26 July 2018; published 8 April 2019)

Electronic tunability in crystals with weakly bound layers can be achieved through layer stacking order. One such example is $MoTe_2$, where the low-temperature orthorhombic T_d phase is topological and host to Weyl quasiparticles. The transition mechanism to the nontrivial topology is elucidated by single-crystal neutron diffraction. Upon cooling from the monoclinic $1T'$ to the T_d phase, diffuse scattering accompanies the transition, arising from random, in-plane layer displacements, and dissipates upon entering the T_d phase. Diffuse scattering is observed only in the $H0L$ plane due to irreversible layer shifts along the c axis that break the centrosymmetry of the monoclinic lattice.

DOI: 10.1103/PhysRevB.99.161105

Transition-metal dichalcogenides are hosts to exotic quantum states, with electronic features that are suitable for optoelectronic and quantum technologies [1,2]. Their crystal structures consist of van der Waals–bound layers, where a change in the layer stacking can result in new properties such as superconductivity, recently observed in bilayer graphene with a "magic" twist angle [3], or transition to the Weyl semimetal state [4–7] reported in the T_d phase of $MoTe_2$ and in the Kooi phase of $Ge_2Sb_2Te_5$ [8]. $MoTe_2$ is a prototype for understanding how stacking variations in layered materials can lead to exotic states of matter. Its crystal structure can be tuned by temperature and pressure between two phases; the topologically trivial $1T'$ phase, and the noncentrosymmetric T_d phase, the host of Weyl quasiparticles. The crystal symmetry is thus essential to predicting the emergence of topologically protected states.

The mechanism of the structural transition has been of particular interest in $MoTe_2$, since Weyl quasiparticles are predicted in the low-temperature phase of the noncentrosymmetric orthorhombic T_d phase, protected by crystal symmetry. Early x-ray diffraction and Raman-scattering measurements suggested that the high-temperature $1T'$ monoclinic structure belongs to the $P2_1/m$ space group that preserves inversion symmetry [9–12]. More recent Raman and second-harmonic generation measurements indicated that the inversion symmetry of the $1T'$ phase is most likely broken in thin films [13].

How the stacking pattern and disorder arise in $MoTe_2$ has implications on many other van der Waals–bound layered materials where stacking can be controlled reproducibly by temperature or pressure. Examples include transitions with pressure in WTe_2 [14], ReS_2 [15], $ReSe_2$ [16], MoS_2 [17–19], and Ta_2NiSe_5 [20]; with temperature in $RuCl_3$ [21], CrX_3 (X = Cl, Br, I) [22], and $CdPS_3$ [23]; and with either temperature or pressure in In_2Se_3 [24,25] and $MoTe_2$ [26]. In $MoTe_2$, the stability of the $1T'$ and T_d phases was explained through density functional theory calculations [27], but the authors of Ref. [27] did not investigate how the transition proceeds.

The difference between $1T'$ and T_d states can be illustrated by considering the nature of the layer stacking. Shown in Figs. 1(a) and 1(d) are the crystal structures of the T_d and $1T'$, respectively. The T_d phase can be thought of as having "AA" layer order, where "A" denotes an operation mapping one layer to the next. For T_d, this operation involves translation along the c axis by 0.5 lattice constants and reflections about the a and b directions. Though there are two layers per unit cell, the operation is the same for both layers. In contrast, the layer stacking of $1T'$ can be described by "AB", where "B" denotes an operation just like "A" but with an additional shift of about ± 0.15 lattice constants along the a direction, where the sign depends on whether the "B" is in an even or odd position in the layer sequence. Though this description of $1T'$ is approximate and neglects additional intralayer distortions relative to the layers in T_d, it captures the binary choice of layer placement at each interlayer boundary. The additional shifts in $1T'$ result in a tilting of the unit cell with a monoclinic angle $\beta \approx 93.9°$. To elucidate the nature of the transition mechanism across the phase boundary, we employed high-resolution single-crystal neutron diffraction. In this Rapid Communication, we show that the diffuse scattering that appears on cooling through the $1T'$ to T_d transition is consistent with random layer shifts, driving the transition from ABAB layer stacking in the $1T'$ phase to AAAA layer stacking in the T_d phase.

The single crystal of $MoTe_2$ was grown in a 1:25 molar ratio of Mo:Te using high-purity elements (99.9999% for both). The elements were heated together in an evacuated silica ampoule to 1050 °C, held there for 24 h, then cooled to 900 °C at a rate of 0.5 °C/h and quenched in liquid nitrogen. The neutron-scattering measurements were performed on the single-crystal diffractometer TOPAZ at Oak Ridge National

*Present address: Department of Physics, Central Michigan University, Mount Pleasant, Michigan 44859.

†Corresponding author: louca@virginia.edu

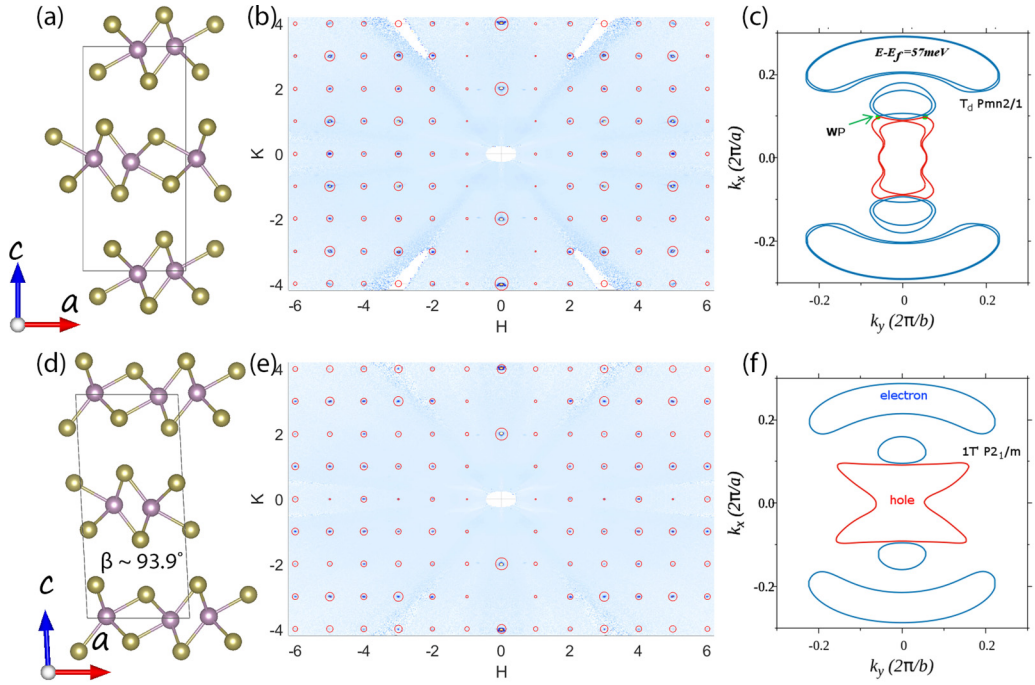

FIG. 1. Shown in (a) and (d) are the refined crystal structures of the T_d and $1T'$ phases of $MoTe_2$. (b) and (e) are neutron-scattering intensity maps of the $HK0$ planes at 100 and 295 K. (c) and (f) are plots in the k_x-k_y plane of the Fermi surface with $k_z \sim 0$ from electronic band structure calculations using the refined parameters of $Pnm2_1$ and $P2_1/m$ structures.

Laboratory. By indexing the Bragg peaks, an orientation matrix (a.k.a. UB matrix) is defined for the data at each temperature. The lattice constants are obtained from the UB matrices. For the 295 and 260 K data, the UB matrices are defined using only the reflections from one of the twin domains. The structure factor of each Bragg reflection is calculated from the reduced and normalized data in order to determine the crystal structure. To accommodate the L-direction elongated peak shape, the intensities of the reflections are taken as integrals over a box of size $0.3 \times 0.3 \times 0.5$ in reciprocal units subtracting the average background in a shell of 0.08 reciprocal unit thickness. Atomic coordinates in this Rapid Communication are defined in the convention typically used for the $1T'$ phase, i.e., $b < a < c$. The lattice parameters are listed in Table I. Data in the form of intensity as a function of momentum transfer in three-dimensional reciprocal space were collected successively at 295, 260, 240, and 100 K, and averaged within $-0.1 \leqslant K \leqslant 0.1$ for the $H0L$ plane and $-0.1 \leqslant H \leqslant 0.1$ for the $0KL$ plane. There are two twins with opposite tilts in the sample. Alignment was done with the dominant twin, which occupies an estimated 85%–90% of the crystal as determined from the ratios of various Bragg peak intensities. Since shearing of layers along the a direction in the ac plane corresponds to a displacement of Bragg peaks and other reciprocal-space features along L in the $H0L$ plane, the Bragg peaks of the minority twin occupy positions of approximately $(H, 0, L - 0.3H)$. We accounted for the domain mosaic spread seen in the $H0L$ plane in our data by convoluting the simulated intensities with a two-dimensional Gaussian having widths in the radial and angular directions increasing linearly in the momentum transfer magnitude $|Q|$, with the mosaic spread estimated to correspond to that of the data. Since the simulated data were calculated for an orthorhombic supercell while the phase at 260 K is monoclinic, the 260 K simulated data were plotted for a monoclinic unit cell with $\beta \approx 93.9°$ by shifting intensities from $(H, 0, L)$ to $(H, 0, L - 0.15H)$. The data plotted in Fig. 3(d) are averaged within ± 0.1 r.l.u. in the H and K directions, subtracted from a background taken as the average of intensities along $(1.8, 0, L)$ and $(2.2, 0, L)$ which were each averaged within 0.05 and 0.1 r.l.u. in the H and K directions, respectively. To correct for misalignment during the temperature change, the simulated intensities were translated uniformly along L to match the data. The data in

TABLE I. Refined atom positions of $MoTe_2$ at 295, 260, 240, and 100 K using $P2_1/m$ (295 and 260 K) and $Pnm2_1$ (240 and 100 K) space group. The lattice constants are $a = 6.33$ Å, $b = 3.48$ Å, $c = 13.82$ Å, $\beta = 93.8°$ (295 K), and $\beta = 93.7°$ (260 K).

	295 K	260 K	240 K	100 K
Mo1 x	0.188(1)	0.191(1)	0.8975(7)	0.8944(6)
z	0.0078(5)	0.0081(6)	0.0001(4)	0.9996(3)
Mo2 x	0.319(1)	0.318(1)	0.5316(7)	0.5288(5)
z	0.5066(5)	0.5062(7)	0.9857(3)	0.9859(2)
Te1 x	0.582(1)	0.579(2)	0.287(1)	0.2838(8)
z	0.1050(6)	0.1052(8)	0.0979(5)	0.0979(4)
Te2 x	0.104(1)	0.107(2)	0.7926(9)	0.7893(7)
z	0.1505(6)	0.1513(7)	0.1416(5)	0.1410(3)
Te3 x	0.556(1)	0.558(2)	0.3589(9)	0.3610(7)
z	0.3512(6)	0.3511(7)	0.3437(4)	0.3444(3)
Te4 x	0.053(1)	0.054(2)	0.856(1)	0.8592(7)
z	0.3955(6)	0.3963(7)	0.3870(5)	0.3873(3)
χ^2	22.28	28.72	6.72	4.94

Fig. 3(e) were averaged similarly to Fig. 3(d), but with the background taken as the average of $(2.8, 0, L)$ and $(3.2, 0, L)$ intensities. For the band structure calculations, we used density functional theory as implemented in the Vienna *Ab initio* Simulation Package (VASP). The details of the calculation are the same as those reported in Ref. [28].

Shown in Fig. 1(b) is a plot of the $(HK0)$ scattering plane for data collected at 100 K in the T_d phase. The Bragg reflections are the dots while the red circles represent the calculated peak intensity. A similar plot is shown in Fig. 1(e) for data collected at 295 K in the $1T'$ phase. The Rietveld refinement was performed on the structure factors extracted from Bragg reflections and the results are summarized in Table I. *Ab initio* calculations were performed on the refined structures of T_d and $1T'$ phases. With $k_z \sim 0$, cuts near the Fermi surface are shown in Figs. 1(c) and 1(f) at $E \sim 57$ meV above the Fermi level, E_F. Weyl nodes, indicated by WP on the plots, are only observed in the T_d phase [Fig. 1(c)], as previously reported, at the intersections of electron and hole pockets [5–7]. In the centrosymmetric $P2_1/m$ symmetry [Fig. 1(f)], Weyl nodes are absent, consistent with previous results as well [5–7]. Thus the emergence of Weyl nodes upon cooling to the T_d phase is tightly linked to the shifting layers, which is discussed next.

A single layer in $MoTe_2$ consists of the transition-metal (Mo) atoms surrounded by the chalcogen (Te) atoms in either trigonal prismatic (2H) or octahedral ($1T'$ and T_d) local environments as shown in Figs. 1(a) and 1(d). The refinement indicates that the $1T'$ to T_d transition that occurs between 260 and 240 K does not affect the local octahedral structure within the monolayer. Instead, the transition is driven by a relative shift of the layers within the *ab* plane, changing the monoclinic unit cell to orthorhombic. The layer shift occurs between two high-symmetry positions. In the $1T'$ phase, the twofold screw rotation along the *b* axis maps each layer to its next-nearest neighboring layer. In the T_d phase, the twofold screw rotation along the *b* axis is broken by the shifting layers, while a new twofold screw rotation along the *c* axis connecting adjacent layers is established.

Figure 2 is a plot of intensity maps from elastic scattering in the $H0L$ and $0KL$ planes. At 295 K, the crystal is in the $1T'$ phase. At 260 K, the crystal is still in the $1T'$ phase, but diffuse scattering streaks are observed along L in the $H0L$ plane. By 240 K the crystal is mostly in the T_d phase, but with some diffuse scattering streaks along L observed in the $H0L$ plane that are less intense than at 260 K. By 100 K, the crystal has transformed into the T_d phase to the point where no diffuse scattering intensity can be observed. The $0KL$ scattering planes shown on the right panels of Fig. 2 show no clear diffuse streaks along L at any temperature, in contrast to the diffuse scattering observed in the $H0L$ plane. Diffuse streaks were also observed about the *c* axis during the $1T'$-T_d transition by earlier x-ray diffraction measurements, but attributed to variations of the β angle with temperature [29], which is different from what we discuss below.

To estimate the degree of stacking disorder during the structural phase transition, we compare the diffuse scattering intensity at 260 and 240 K to the results from a model of stacking disorder that we describe below. Both the $1T'$ [26] and T_d [9] phases can be constructed by stacking variants of a

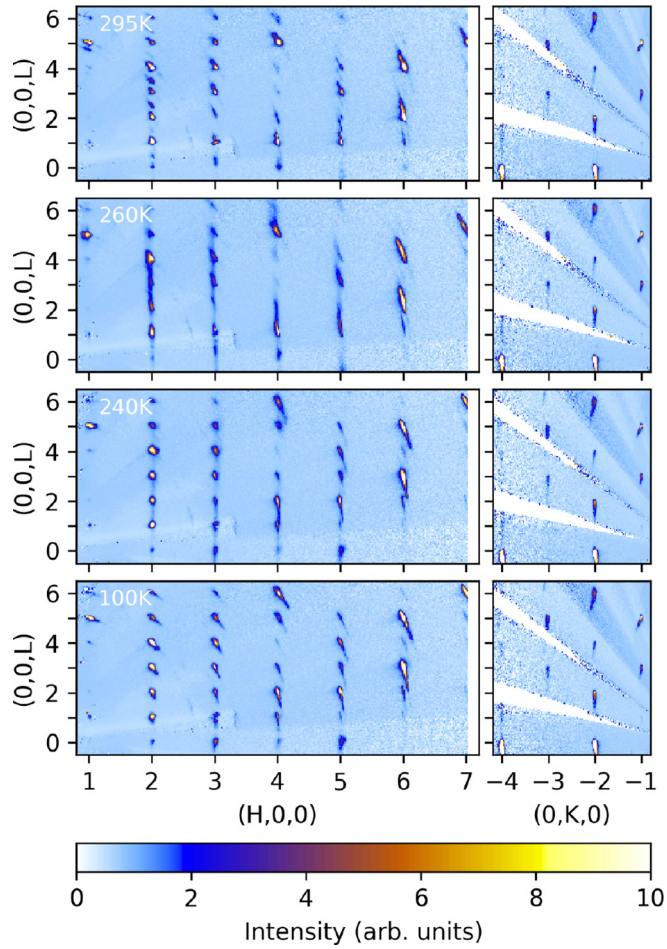

FIG. 2. Neutron-scattering intensity maps of the $H0L$ and $0KL$ planes. Diffuse scattering streaks appear along L in the $H0L$ plane only, upon cooling from 295 to 240 K. By comparison, in the $0KL$ plane, no diffuse streaks are observed.

"base" layer, ignoring the slight differences in atomic coordinates within each layer between the T_d and $1T'$ phases. Each phase can be built from a sequence of stacking operations, "AAAAAA..." for T_d and "ABABAB..." for $1T'$ [Fig. 3(a)]. Operation A reflects about the *a* direction and translates by 0.5 lattice constants along the *b* and *c* direction. Operation B is the same as operation A but with an additional translation along the *a* axis by ± 0.15 lattice constants, with the direction alternating from one layer to the next. The change in *a*-direction displacements results in the orthorhombic T_d phase becoming monoclinic in $1T'$.

For modeling the diffuse scattering, we start from the $1T'$ stacking sequence ABABAB..., then randomly replace B boundaries with A boundaries with probability *p*. Although this model is crude, it allows us to verify that disordered A/B stacking does indeed explain the diffuse scattering reasonably well, and to estimate the amount of stacking defects at 260 and 240 K. A supercell is constructed with a large number of layers, and the intensity is taken as the square of the neutron-scattering structure factor (with the Debye-Waller factor neglected for simplicity) [30], then convoluted with a Gaussian function to mimic resolution effects and changes in the mosaic

spread. The diffuse scattering corresponds to intensities at fractional L as defined in T_d-cell reciprocal lattice units. We note that only disorder for displacements along the b axis would contribute to diffuse scattering in the $0KL$ plane, which suggests that the lack of clear diffuse scattering streaks in the $0KL$ planes in Fig. 2 implies that there is little to no disorder along the b direction. We also note that, since the additional a-axis displacements are multiples of $0.15 \approx 1/6$, the contribution to the diffuse scattering along $(60L)$ is likely to be small. We indeed see little diffuse scattering along $(60L)$, so the data appear to be consistent with our model. (Details on the relation between displacements along specific axes and diffuse scattering in specific planes can be found in the Supplemental Material [31]).

Simulated $H0L$-plane intensity maps are shown in Fig. 3(b) (260 K) and Fig. 3(c) (240 K). Both simulations were based on a 1000-layer supercell where a $1T'$ crystal with two twins having volume fractions of 87% and 13% has B boundaries replaced by A boundaries with probability $p = 0.3$ at 260 K and $p = 0.8$ at 240 K. The model describes well the overall pattern of diffuse scattering in the $H0L$ plane; for example, similar diffuse scattering streaks are seen along $(20L)$, $(30L)$, and most of $(40L)$, while $(60L)$ and $(70L)$ are relatively clean. A closer look at the comparison between the data at 260 K and the model along $(20L)$ is shown in Fig. 3(d), again with calculations using a 1000-layer supercell and $p = 0.3$. There is very good agreement between the model and data, with discrepancies likely due to either varying the distribution of domain orientation or due to inhomogeneities (different regions of the crystal having varying values of p).

For the 240 K data shown in Fig. 3(e), we compare the intensity along $(30L)$ to two models. Model #1 is the model described above with $p = 0.8$. Model #2 is a similar model but starting from the T_d phase stacking and replacing A boundaries with B boundaries with probability $p = 0.1$. Both calculations used 4000 layers. These two models are motivated by different schemes of the $1T'$ to T_d transition. Model #1 assumes B to A transitions are one-way and irreversible, whereas model #2 is motivated by a transition scenario involving fluctuating layers which can shift back and forth but have an average probability of occupation at a certain position. Our data are more consistent with the first model than the second. First, we would expect the intensity upon $(H, 0, L)$ to $(H, 0, -L)$ to be symmetric in model #2 but not in model #1. (See Supplemental Material for further details [31].) Although our data do not match perfectly with either model, intensities in the $H0L$ plane appear to lack L-reflection symmetry, in particular intensities near $(3, 0, -0.5)$ and $(3, 0, 0.5)$ in Fig. 3(e). Second, one would expect the distribution of twin domains to become more equal if A to B fluctuations were to occur with a significant probability, but our analysis suggests the estimated 87%–13% distribution of twin domains at 295 K is most likely true at 260 K as

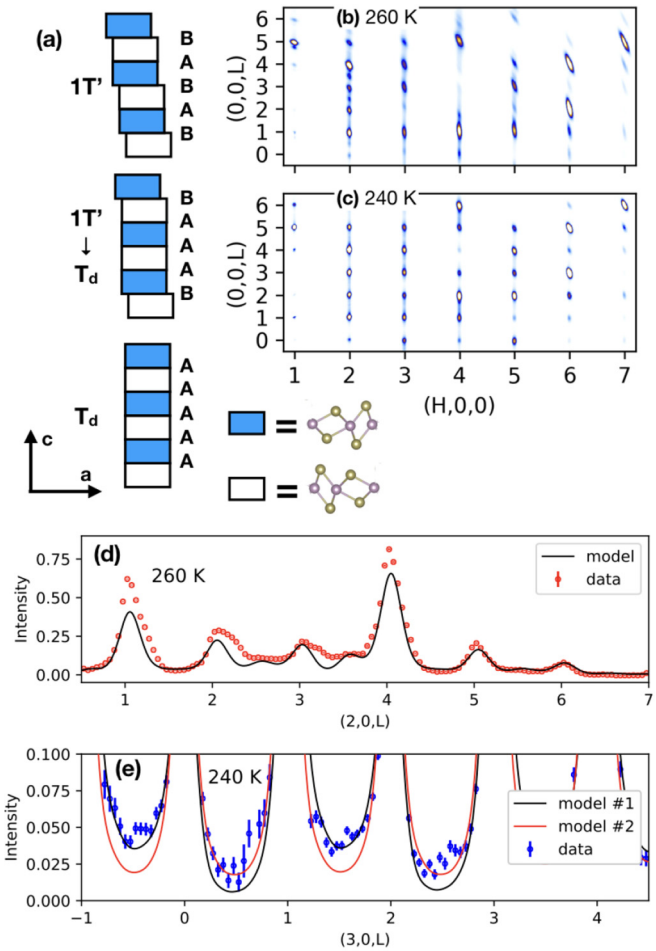

FIG. 3. (a) A schematic diagram describing the model used to explain the diffuse scattering. (b),(c) Simulated $H0L$ intensity maps for 260 K in (b) and 240 K in (c). (d) Comparison of model and data along $(20L)$ at 260 K. (e) Comparison of the diffuse scattering along $(30L)$ at 240 K and the results of the same model as for (c) (#1), with a second model (#2).

well. To conclude, our layer stacking models can explain the diffuse scattering across the transition where the shift of the layers along the a axis is coupled with Weyl node creation or annihilation. It is this layer shift that breaks the twofold screw rotation along the b axis and establishes a new twofold screw rotation along c. This work may stimulate further studies to determine exactly at which angle and layer sequencing Weyl nodes are created or annihilated.

This work has been supported by the Department of Energy, Grant No. DE-FG02-01ER45927. A portion of this research used resources at the Spallation Neutron Source, a DOE Office of Science User Facility operated by the Oak Ridge National Laboratory.

[1] Q. H. Wang, K. Kalantar-Zadeh, A. Kis, J. N. Coleman, and M. S. Strano, Nat. Nanotechnol. **7**, 699 (2012).

[2] D. Jariwala, V. K. Sangwan, L. J. Lauhon, T. J. Marks, and M. C. Hersam, ACS Nano **8**, 1102 (2014).

[3] Y. Cao, V. Fatemi, S. Fang, K. Watanabe, T. Taniguchi, E. Kaxiras, and P. Jarillo-Herrero, Nature (London) **556**, 43 (2018).
[4] L. Huang, T. M. McCormick, M. Ochi, Z. Zhao, M. Suzuki, R. Arita, Y. Wu, D. Mou, H. Cao, J. Yan, N. Trivedi, and A. Kaminski, Nat. Mater. **15**, 1155 (2016).
[5] Y. Sun, S. C. Wu, M. N. Ali, C. Felser, and B. Yan, Phys. Rev. B **92**, 161107(R) (2015).
[6] A. A. Soluyanov, D. Gresch, Z. Wang, Q. Wu, M. Troyer, X. Dai, and B. A. Bernevig, Nature (London) **527**, 495 (2015).
[7] S.-Y. Xu, I. Belopolski, N. Alidoust, M. Neupane, G. Bian, C. Zhang, R. Sankar, G. Chang, Z. Yuan, C.-C. Lee, S.-M. Huang, H. Zheng, J. Ma, D. S. Sanchez, B. Wang, A. Bansil, F. Chou, P. P. Shibayev, H. Lin, S. Jia, and M. Z. Hasan, Science **7**, 613 (2015).
[8] B. J. Kooi and T. M. De Hosson, J. Appl. Phys. **92**, 3584 (2002).
[9] E. Lifshitz, A. H. Francis, and R. Clarke, Solid State Commun. **45**, 273 (1983).
[10] F. Ke, C. Liu, Y. Gao, J. Zhang, D. Tan, Y. Han, Y. Ma, J. Shu, W. Yang, B. Chen, H. K. Mao, X. J. Chen, and C. Gao, Appl. Phys. Lett. **104**, 212102 (2014).
[11] J. Zhao and L. Yang, J. Phys. Chem. C **118**, 5445 (2014).
[12] Y. Qi, P. G. Naumov, M. N. Ali, C. R. Rajamathi, W. Schnelle, O. Barkalov, M. Hanfland, S. C. Wu, C. Shekhar, Y. Sun, V. Süß, M. Schmidt, U. Schwarz, E. Pippel, P. Werner, R. Hillebrand, T. Forster, E. Kampert, S. Parkin, R. J. Cava, C. Felser, B. Yan, and S. A. Medvedev, Nat. Commun. **7**, 11038 (2016).
[13] H.-J. Kim, S.-H. Kang, I. Hamada, and Y.-W. Son, Phys. Rev. B **95**, 180101(R) (2017).
[14] B. E. Brown, Acta Crystallogr. **20**, 268 (1966).
[15] H. Sakai, K. Ikeura, M. Saeed Bahramy, N. Ogawa, D. Hashizume, J. Fujioka, Y. Tokura, and S. Ishiwata, Sci. Adv. **2**, 1601378 (2016).
[16] S.-Y. Chen, T. Goldstein, D. Venkataraman, A. Ramasubramaniam, and J. Yan, Nano Lett. **16**, 5852 (2016).
[17] K. Zhang, C. Bao, Q. Gu, X. Ren, H. Zhang, K. Deng, Y. Wu, Y. Li, J. Feng, and S. Zhou, Nat. Commun. **7**, 13552 (2016).
[18] R. Beams, L. Gustavo Canado, S. Krylyuk, I. Kalish, B. Kalanyan, A. K. Singh, K. Choudhary, A. Bruma, P. M. Vora, F. Tavazza, A. V. Davydov, and S. J. Stranick, ACS Nano **10**, 9626 (2016).
[19] Y. Zhou, X. Chen, N. Li, R. Zhang, X. Wang, C. An, Y. Zhou, X. Pan, F. Song, B. Wang, W. Yang, Z. Yang, and Y. Zhang, AIP Adv. **6**, 075008 (2016).
[20] D. Zhou, Y. Zhou, C. Pu, X. Chen, P. Lu, X. Wang, C. An, Y. Zhou, F. Miao, C. H. Ho, J. Sun, Z. Yang, and D. Xing, npj Quantum Mater. **2**, 19 (2017).
[21] P. G. Naumov, M. A. ElGhazali, H. Mirhosseini, V. Süß, E. Morosan, C. Felser, and S. A. Medvedev, J. Phys.: Condens. Matter **30**, 035401 (2018).
[22] L. Hromadova, R. Martonak, and E. Tosatti, Phys. Rev. B **87**, 144105 (2013).
[23] Z. H. Chi, X. M. Zhao, H. Zhang, A. F. Goncharov, S. S. Lobanov, T. Kagayama, M. Sakata, and X. J. Chen, Phys. Rev. Lett. **113**, 036802 (2014).
[24] A. P. Nayak, S. Bhattacharyya, J. Zhu, J. Liu, X. Wu, T. Pandey, C. Jin, A. K. Singh, D. Akinwande, and J. F. Lin, Nat. Commun. **5**, 3731 (2014).
[25] A. Nakano, K. Sugawara, S. Tamura, N. Katayama, K. Matsubayashi, T. Okada, Y. Uwatoko, K. Munakata, A. Nakao, H. Sagayama, R. Kumai, K. Sugimoto, N. Maejima, A. Machida, T. Watanuki, and H. Sawa, IUCrJ **5**, 158 (2018).
[26] A. Glamazda, P. Lemmens, S.-H. Do, Y. S. Kwon, and K.-Y. Choi, Phys. Rev. B **95**, 174429 (2017).
[27] M. A. McGuire, H. Dixit, V. R. Cooper, and B. C. Sales, Chem. Mater. **27**, 612 (2015).
[28] J. Yang, J. Colen, J. Liu, M. C. Nguyen, G.-W. Chern, and D. Louca, Sci. Adv. **3**, eaao4949 (2017).
[29] R. Clarke, E. Marseglia, and H. P. Hughes, Philos. Mag. B **38**, 121 (1978).
[30] G. Shirane, S. M. Shapiro, and J. M. Tranquada, *Neutron Scattering with a Triple-Axis Spectrometer* (Cambridge University Press, Cambridge, UK, 2002).
[31] See Supplemental Material at http://link.aps.org/supplemental/10.1103/PhysRevB.99.161105 for a discussion on how the structure factors were extracted from the single-crystal diffraction pattern and the mathematical details of the structural phase transition model used in this Rapid Communication.